Effects of anchoring and arc structure on the control authority of a rail plasma actuator

IOP Publishing Journal of Physics D: Applied Physics
J. Phys. D: Appl. Phys. **50** (2017) 355203 (13pp) https://doi.org/10.1088/1361-6463/aa7e65

Effects of anchoring and arc structure on the control authority of a rail plasma actuator

Young-Joon Choi, Miles Gray, Jayant Sirohi and Laxminarayan L Raja

Department of Aerospace Engineering and Engineering Mechanics, The University of Texas at Austin, Austin, TX, United States of America

E-mail: lraja@mail.utexas.edu

Received 3 May 2017, revised 2 July 2017
Accepted for publication 7 July 2017
Published 10 August 2017

Abstract

Experiments were conducted on a rail plasma actuator (RailPAc) with different electrode cross sections (rails or rods) to assess methods to improve the actuation authority, defined as the impulse generated for a given electrical input. The arc was characterized with electrical measurements and high-speed images, while impulse measurements quantified the actuation authority. A RailPAc power supply capable of delivering ∼1 kA of current at ∼100 V was connected to rod electrodes (free-floating with circular cross-section) and rail electrodes (flush-mounted in a flat plate with rectangular cross-section). High-speed images show that the rail electrodes cause the arc to anchor itself to the anode electrode and transit in discrete jumps, while rod electrodes permit the arc to transit smoothly without anchoring. The impulse measurements reveal that the anchoring reduces the actuation authority by ∼21% compared to a smooth transit, and the effect of anchoring can be suppressed by reducing the gap between the rails to 2 mm. The study further demonstrates that if a smooth transit is achieved, the control authority can be increased with a larger gap and larger arc current. In conclusion, the actuation authority of a RailPAc can be maximized by carefully choosing a gap width that prevents anchoring. Further study is warranted to increase the RailPAc actuation authority by introducing multiple turns of wires beneath the RailPAc to augment the induced magnetic field.

Keywords: plasma, actuator, impulse, railgun, control authority, magnetohydrodynamic

(Some figures may appear in colour only in the online journal)

1. Introduction

Plasma actuators have been proposed for active flow control applications due to their low mass, compact volume, high reliability, and fast response time [1, 2]. These devices can be separated into three types: electrohydrodynamic (EHD), magnetohydrodynamic (MHD), and thermal, depending on the interaction mechanism between the plasma and the surrounding flow. EHD actuators induce directional momentum transfer to the surrounding air through electric field forcing in a glow discharge region [3–6]. MHD actuators transfer momentum through a body force produced by coupling between an external or self-induced magnetic field and a moving arc [7, 8]. Thermal actuators disturb the surrounding flow due to rapid dilatation caused by formation of the high temperature plasma [9–11].

Although numerous plasma actuator concepts have demonstrated flow control ability in laboratory experiments [12–14], their application in full-scale aircraft has not yet been realized. Measurements showed that plasma actuators have low control authority (defined as the momentum delivered by the actuator to the surrounding air), such that their operation in a full-scale environment has little effect on the flow field at realistic Reynolds and Mach numbers. In the case of an EHD actuator, such as a dielectric barrier discharge (DBD) plasma actuator, studies point towards a performance barrier imposed

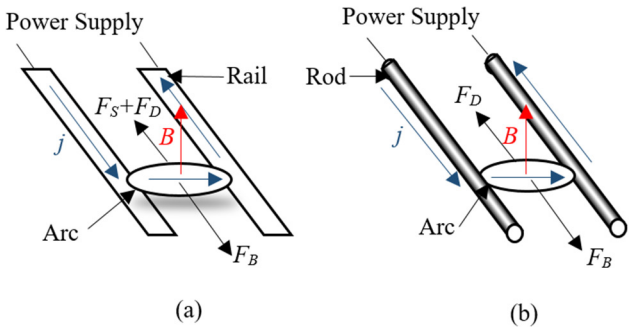

Figure 1. RailPAc configuration for (a) rail and (b) rod case.

by the low interaction parameter between the discharge and neutral air regions, as well as a physical limitation imposed by charge deposition on its dielectric surface [15, 16]. These deficiencies limited the effectiveness of DBD actuators to low Reynolds number regimes ($\sim 10^5$). Clearly, a novel approach is required that can preserve all the benefits of plasma actuators and is relevant in full-scale flow control applications.

A MHD actuator based on a railgun concept has demonstrated potential to increase the actuation authority of plasma actuators. [17]. We propose that the same physical principle that can accelerate a railgun projectile to several km/s can be harnessed to increase the actuation authority of plasma actuators. The actuation authority can be increased by generating a large MHD body force in the discharge region that transfers large momentum to the surrounding air. In addition, the lack of moving parts permit these devices to operate on a wide bandwidth and effectively influence the natural instabilities of the flow. The concept was demonstrated in the form of a rail plasma actuator (RailPAc), shown in figure 1(a). This device consists of parallel rails (electrodes) flush mounted to an insulating surface. When a high current ($\sim$1 kA) is supplied at low voltage ($\sim$100 V), an arc is formed. A self-induced magnetic field ($\vec{B}$) is generated that couples with the arc current density ($\vec{j}$) to impart a Lorentz force ($\vec{F_B}$), which accelerates the arc. The resulting arc motion transfers momentum to the surrounding air.

Several RailPAc studies have assessed its potential for flow control applications. Pafford *et al* [17] measured $\sim$10 m/s induced velocity in the boundary layer region of an airfoil operating at Re $\sim$ 450 000. Choi *et al* [18] expanded upon this work with particle imaging velocimetry on a RailPAc operating in quiescent air to capture the large scale flow disturbance caused by a propagating arc. Their measurements revealed that the moving arc pushes air ahead of its transit through compression, while a high temperature wake region is created behind the transit. The surrounding air is entrained into the wake region, such that a directional jet in the propagation direction is generated after the transit. In addition to the induced velocity measurements, Choi *et al* [19] quantified the RailPAc control authority through transient force and impulse measurements and identified the actuator's ability to produce a large and scalable body force. A peak transient force of $\sim$0.4 N imparting a peak impulse of $\sim$0.68 mN s was measured in that study. It was also revealed that the body force scales quadratically with the arc current and the impulse scales linearly with the discharged energy, suggesting that the actuator can be tailored to a specific flow condition by simply changing the electrical characteristics.

While all these studies demonstrate the actuator's capability to induce a large flow field disturbance, the experiments also identified the complex arc shape as a limiting factor in RailPAc control authority. The high-speed images of the arc transit [17, 19] show that the arc roots, or regions where the arc attaches to the electrode surfaces, behave differently on the anode and cathode. Although the motion of anode root along the electrode can be characterized as discrete jumps, the cathode root moves smoothly along the electrode. This phenomenon was defined by Gray *et al* [20, 21] as the "anchoring" behavior, and Choi *et al* [19] hypothesized that the actuation authority and efficiency of a RailPAc can be improved by preventing the asymmetric transit of the arc roots. Based on this hypothesis, Gray *et al* [21] further investigated some mechanisms to suppress anchoring in the arc transit. By examining the internal structure of a propagating arc, they attributed anchoring to the absence of interaction between the cathode and anode roots. Their high-speed images identified the arc as two distinct jets issuing from the cathode and anode roots. When the flush mounted rails are spaced closely together ($\sim$2 to $\sim$3 mm), each jet is directed towards the opposite arc root, and a smooth transit of the anode root can be observed. However, if the rails are spaced far apart ($\sim$12 mm), the jets form vertical columns that behave independently from one another. These observations reveal that the presence of a dielectric gap in a flush mounted case prevents strong interaction between the two arc roots. The anchoring phenomenon can be suppressed if the interaction is enhanced by minimizing the separation distance between the arc roots.

The objective of this paper is to study the effect of anchoring and electrode geometry on the actuation authority of a RailPAc. The effect of anchoring on actuation authority can be quantified by comparing the impulse measured on a RailPAc with anchored transit versus a smooth transit. This study applies two methods to prevent anchoring in the arc transit. In one case, smooth transit is achieved by constructing a RailPAc out of free-floating rods, as shown in figure 1(b), that remove the insulating gap to increase the interaction between the arc jets. In another case, the gap spacing of the configuration shown in figure 1(a) is decreased to a small distance until smooth transit of the anode root is achieved. By changing the separation distance between the electrodes, the effect of electrode geometry on the RailPAc control authority can also be quantified.

2. Actuation mechanism

To illustrate the effect of volumetric Lorentz force ($\vec{f_B}$) on the fluid momentum per unit volume (ρu), consider a control volume (figure 2) and momentum equation in the propagation direction ($\hat{e}_x$-direction),

$$\frac{\partial}{\partial t}\int_{\forall}\rho u\,\mathrm{d}\forall+\int_S\rho(\vec{v}\cdot\vec{n})\,\mathrm{d}s=\int_{\forall}\vec{f_B}\cdot\hat{e}_x\,\mathrm{d}\forall-\int_S\vec{\tau}\cdot\vec{n}\,\mathrm{d}S-\int_S\vec{p}\cdot\vec{n}\,\mathrm{d}S. \quad (1)$$

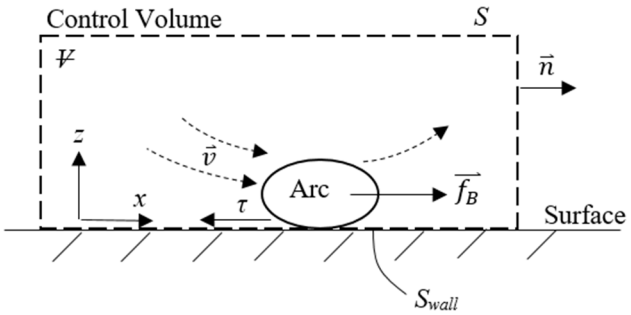

Figure 2. Control volume analysis for RailPAc.

Let the control volume be sufficiently large compared to the actuator dimensions, so that the surface flux integral (with shear stress, τ) as well as the integral over the pressure disturbances (p) at the boundary evaluates to zero. Then, the integral over the fluid momentum over the actuation time (0 to T) is given by,

$$\int_0^T \frac{\partial}{\partial t}\int_{\mathcal{V}} \rho u \,\mathrm{d}\mathcal{V}\,\mathrm{d}t = \int_0^T \left[\int_{\mathcal{V}} \vec{f_B}\cdot\hat{e}_x \,\mathrm{d}\mathcal{V} - \int_{S_{\mathrm{wall}}} \tau\cdot\vec{n}\,\mathrm{d}S\right]\mathrm{d}t. \tag{2}$$

If the change in the fluid momentum within the control volume is defined as $\Delta\Theta$, impulse due to Lorentz force is J_B, and impulse due to surface drag (from viscous interaction with the wall) is J_S, the momentum integral equation can be rewritten as,

$$\Delta\Theta = J_B - J_S. \tag{3}$$

By considering a large control volume, equation (1) simplifies to equation (3), which clearly shows that the Lorentz force results in momentum increase of the flow. In addition, the impulse imparted to the flow can be gauged if the impulse delivered by the Lorentz force is measured, even if the details of the induced velocity ($\vec{v}$) is unknown. Note that the drag force arises due to the proximity of the arc to the RailPAc mounting surface and the electrodes. The drag force is small in rod electrodes because the contact area is small. In the case of rail electrodes, the drag force is negligible compared to the Lorentz force, since the arc deflects away from the mounting surface.

The Lorentz force term can be obtained from the Lorentz force law,

$$\vec{f_B} = q\vec{E} + \vec{j}\times\vec{B}. \tag{4}$$

If the component of Lorentz force in the propagation direction is considered, the contribution from electric field ($q\vec{E}$) is zero since it is perpendicular to the arc propagation direction. Note also that the sign of the Lorentz force is always positive, since the force always acts in the direction of the arc motion ($\hat{e}_x$-direction). While equation (4) gives the exact distribution of the volumetric Lorentz force, the spatial distributions of magnetic field as well as current density are difficult to obtain analytically or experimentally. Instead, Lorentz force can be expressed in terms of inductance by relating the virtual work done by Lorentz force (δW) to the change in the magnetic potential energy of the RailPAc (δU) [22],

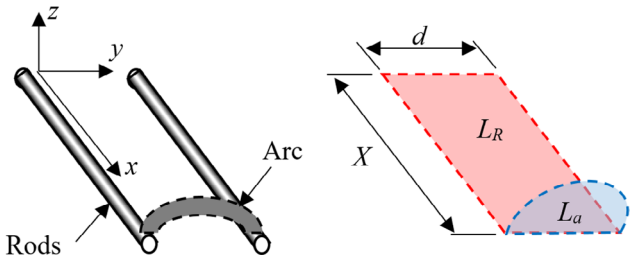

Figure 3. Inductance decomposition into sum of contribution from rod geometry (L_R) and arc shape (L_a).

$$\delta W = \delta U. \tag{5}$$

Consider a deformable arc situated at some X location along the electrodes (figure 3). The total Lorentz force acting on the arc can be evaluated at an X location by integrating the volumetric force over the arc length and arc cross section (A),

$$F_B(X) = \int_0^l \hat{X}\cdot\vec{f_B}A\mathrm{d}\zeta. \tag{6}$$

By considering a variation in coordinate, δX, along the propagation direction, the virtual work done by the Lorentz force is given by,

$$\delta W = F_B(X)\delta X. \tag{7}$$

Note from figure 3 that the discharge current from a RailPAc power supply forms a single loop inductor with inductance, L, consisting of current loop through the electrodes and the arc. Let us decompose the inductance into two terms: inductance contribution from electrode geometry (L_R) and contribution from arc shape (L_a). Then, the total magnetic energy can be expressed in terms of arc current (I) by,

$$U = \frac{1}{2}(L_R + L_a)I^2. \tag{8}$$

The change in magnetic energy due to arc motion and deformation can be expressed as,

$$\delta U = U(X+\delta X) - U(X). \tag{9}$$

Such that the Lorentz force in the propagation direction is given by,

$$F_B(X) = \frac{1}{2}\left(\frac{\partial L_R}{\partial X} + \frac{\partial L_a}{\partial X}\right)I^2. \tag{10}$$

The term $\frac{\partial L_R}{\partial X}$ is known as the inductance gradient based on the electrode geometry. This constant is commonly used in railgun studies to estimate the Lorentz force based on the armature current [23]. However, the armature of a railgun is a solid body of constant geometry, while a RailPAc has deformable plasma arc as an armature. Due to changes in the arc shape during its transit, the inductance gradient of a RailPAc has an additional term, $\frac{\partial L_a}{\partial X}$. This term describes the changes in the RailPAc force due to elongation and contraction of the arc. Hence, the RailPAc inductance gradient is comprised of time invariant term ($\frac{\partial L_R}{\partial X}$) and time variant term ($\frac{\partial L_a}{\partial X}$) that complicates the modeling of RailPAc inductance gradient.

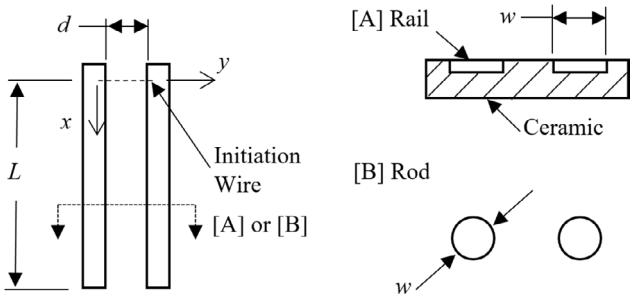

Figure 4. RailPAc configuration for rod and rail cases.

Instead, a nominal inductance gradient ($\bar{L}'$) can be obtained experimentally by integrating equation (10) in time,

$$J_B = \int_0^T F_B \mathrm{d}t = \frac{1}{2}\bar{L}' \int_0^T I^2 \mathrm{d}t. \tag{11}$$

Equation (11) shows that the impulse delivered by the RailPAc is linearly proportional to the action integral ($\int_0^T I^2 \mathrm{d}t$) [24] scaled by the time averaged inductance gradient.

The control volume analysis revealed that the body force produced by RailPAc can increase the fluid momentum, and the momentum increase can be quantified by measuring the impulse based on Lorentz force (J_B). Furthermore, equation (11) provided a convenient scalar ($\bar{L}'$) to compare the actuation authority of different RailPAc configurations.

A low natural frequency test stand has been used by several authors in the past to measure the impulse produced by plasma propulsion devices [25] and actuators [19, 26] with Lorentz force acting over short time scales. This study follows a similar methodology by mounting a RailPAc to a suitable test stand and measuring the impulse delivered by a RailPAc. If the measured impulse is compared to the action integral, the inductance gradient of a particular RailPAc configuration can be obtained. By comparing the changes in the inductance gradient to the arc morphology, the effect of anchoring and electrode geometry can be quantified. Therefore, this paper will discuss methodologies employed to quantify the inductance gradient and results obtained from high-speed imaging, electrical, and impulse measurements.

3. Experimental methods

The experimental setup is comprised of a RailPAc and a power supply circuit mounted on an impulse test stand. Figure 4 describes the RailPAc geometry for rail and rod electrodes. In the rail case, parallel copper bars are flush mounted to a ceramic surface. For the rod case, tungsten rods are mounted in mid-air in a second test setup.

Rail or rod electrodes (152 mm length) are spaced at different distances as tabulated in table 1. The rod diameter (3.175 mm) as well as the rail width (6.35 mm) are denoted by w. The rails have a thickness of 0.56 mm. Note that each RailPAc configuration is labeled with a distinct identifier. For example, a RailPAc consisting of flush-mounted rails that are spaced 12.7 mm apart is labeled A13. Similarly, a RailPAc comprised of parallel rods separated by 2.0 mm is labeled B02. Each configuration will be referred to by its identifier for clarity.

Table 1. Summary of RailPAc configurations and dimensions.

Case	Shape	d (mm)	w (mm)	l (mm)
A13	Rail	12.7	6.35	152
A02	Rail	2.0	6.35	152
B13	Rod	12.7	3.175	152
B06	Rod	6.4	3.175	152
B02	Rod	2.0	3.175	152

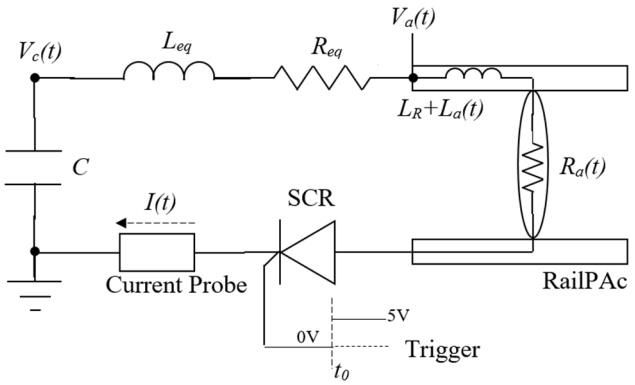

Figure 5. Electrical schematic of a RailPAc power supply circuit.

As shown in figure 4, an aluminum fuse wire situated 25 mm away from one end of the electrode initiates the arc at a consistent location. The location of the initiation wire and the electrode length limited the arc transit distance (l) to 127 mm.

3.1. High-speed imaging

Two Phantom Miro M-310 cameras were used to capture the front view and top view of the arc transit. Lenses with 100 mm focal length and f-stop of f/30 were installed to reduce image saturation from plasma emission. The videos were captured at 20 000 fps with exposure time of 1 μs.

3.2. Electrical measurements

The RailPAc power supply (figure 5) consists of a capacitor bank ($C = 3.55$ mF), equivalent inductance ($L_{eq} = 12.4$ μH), equivalent circuit resistance (R_{eq}), and a silicon controlled rectifier (SCR) connected in series. The capacitor is charged using an external power supply (Xantrex XHR 600) to different initial voltages ($V_{ci} = 160$ V to 240 V) to control the current as well as energy delivered to the arc. Initially, an aluminum fuse wire bridges the gap between the rails and the capacitor discharge is impeded by the SCR. When a trigger voltage is sent to the SCR at an initiation time (t_0), a large current discharges through the circuit and an arc is formed by the vaporization of the aluminum fuse wire. As the self-induced Lorentz force begins to accelerate the arc, the motion as well as the deformation of the arc changes the inductance and resistance of the RailPAc circuit. The circuit can be modeled as a second order non-linear differential equation of the form,

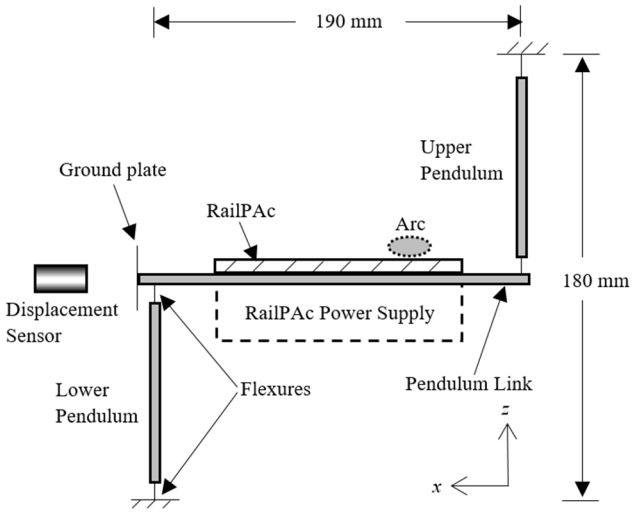

Figure 6. Impulse test stand schematic.

$$\ddot{q} + \frac{R_{\mathrm{eq}} + R_a(\dot{q})}{L_{\mathrm{eq}} + L_R + L_a(t)}\dot{q} + \frac{1}{(L_{\mathrm{eq}} + L_R + L_a(t))C}q = 0 \qquad (12)$$

where q is the charge. The total resistance of the RailPAc circuit is the sum of fixed circuit resistance (R_{eq}) and variable arc resistance (R_a). The total inductance is sum of fixed inductance ($L_{\mathrm{eq}} + L_R$) and variable RailPAc inductance (L_a) as a result of arc motion and deformation. The variable RailPAc inductance can be obtained by multiplying the inductance gradient of the RailPAc with the arc location along the electrodes. Choi *et al* [19] showed that the change in the total inductance due to the arc motion ($L_R + L_a$) is small compared to the fixed inductance of the circuit and therefore can be neglected.

High voltage probes were used to measure the capacitor voltage (V_c) and rail voltage (V_a). The arc current (I) was measured using a Hall effect current probe (Tamura L06P800-05), or a Pearson probe for current exceeding 1.1 kA.

The variable arc resistance (R_a) was measured by dividing the rail voltage by the arc current as a function of time. The total energy delivered by the capacitor (E) was computed based on the initial (V_{ci}) and final (V_{cf}) capacitor voltages.

$$E = \frac{C}{2}(V_{\mathrm{ci}}^2 - V_{\mathrm{cf}}^2). \qquad (13)$$

The arc energy (E_a) was obtained by multiplying the arc voltage with the arc current and integrating the product over the arc transit duration. Note that the sum of the arc energy and energy dissipated by the circuit resistance is equal to the total energy.

3.3. Impulse measurements

A low natural frequency test stand shown in figure 6 was built to characterize a RailPAc impulse. This compact pendulum [27] consists of an upper pendulum and an inverted lower pendulum mechanically coupled via a rigid pendulum link (aluminum honeycomb plate). A RailPAc is mounted on top of the rigid link, while a RailPAc power supply is situated below the link. Brass flexures act as hinges of the upper pendulum and conductive paths to charge the capacitor bank from an external power supply. The plastic flexures of the lower pendulum reduce the flexure stiffness and electrically isolate the test stand from the base. The test stand displacement was measured using a capacitive displacement sensor (capaNCDT 6110 CS05) with 0.5 mm range and 75 nm resolution. A copper ground plate was mounted at the lower pendulum end of the rigid link and served as a target plane for the displacement sensor.

When the RailPAc arc experiences Lorentz force, an equal and opposite reaction force will be imparted on the RailPAc and the impulse test stand. However, if electrical wires carry current in and out of the impulse test stand, the reaction force experienced by the test stand does not always equal the Lorentz force experienced by the arc. The measurement error introduced by improper arrangement of electrical wires led to several studies [28–30] that attempted to characterize the reaction force from the Lorentz force, but obtained conflicting results. The issue can be circumvented by mounting the entire RailPAc assembly on a test stand. If the setup is electrically isolated within the impulse test stand, only the reaction force from the arc will be imparted on the test stand.

The impulse applied to a test stand can be measured from the displacement (x_I),

$$x_I(t) = \frac{J}{m_{\mathrm{eq}}\omega_d}\mathrm{e}^{-\zeta\omega_d t}\sin(\omega_n t) \qquad (14)$$

where, J is the total impulse delivered to the test stand by the RailPAc, ω_d and ω_n are damped and undamped natural frequencies, m_{eq} is the equivalent mass of the test stand, and ζ is the damping ratio. If the damping ratio is sufficiently small, the maximum displacement can be approximated as,

$$\delta_{\max} \approx \frac{J}{m_{\mathrm{eq}}\omega_d}. \qquad (15)$$

Equation (15) shows that the maximum displacement of the test stand is linearly proportional to the impulse delivered. Thus, if the proportionality coefficient ($m_{\mathrm{eq}}\omega_d$) is known, then the impulse can be measured from the maximum displacement of the test stand.

The natural frequency of the compact pendulum test stand can be made arbitrarily small by shifting the center of mass of the rigid link towards the lower pendulum. For this test stand, the center of mass was set by distributing the RailPAc power supply mass (572.4 g) towards the lower pendulum. This mass was larger than the equivalent mass contribution from the pendulum link and arms (310.3 g) as well as the RailPAc mass ($80 \sim 100$ g). Note that the exact RailPAc mass varied dependent upon the particular rail or rod geometry and the natural frequency was approximately 0.7 Hz.

The impulse test stand was calibrated using an impact pendulum setup shown in figure 7. An aluminum impactor with steel impact tips at its ends was suspended from two nylon threads. Initially, the horizontal pendulum was displaced from its equilibrium position using an electromagnet. When the electromagnet current was interrupted, the impactor was released and subsequently collided inelastically with the pendulum link.

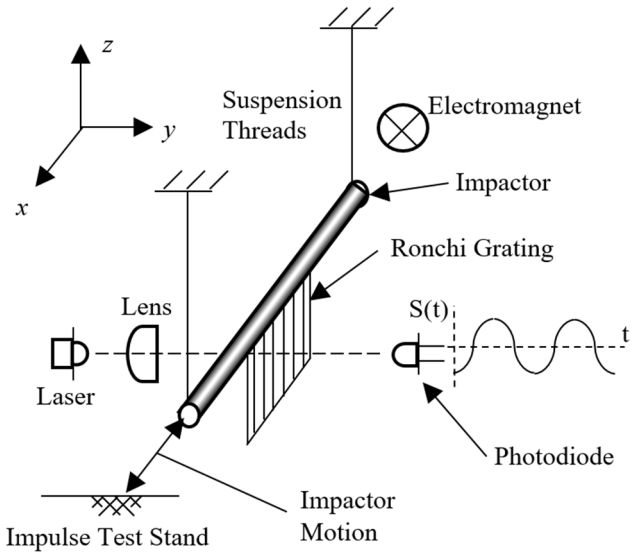

Figure 7. Impulse test stand calibration setup.

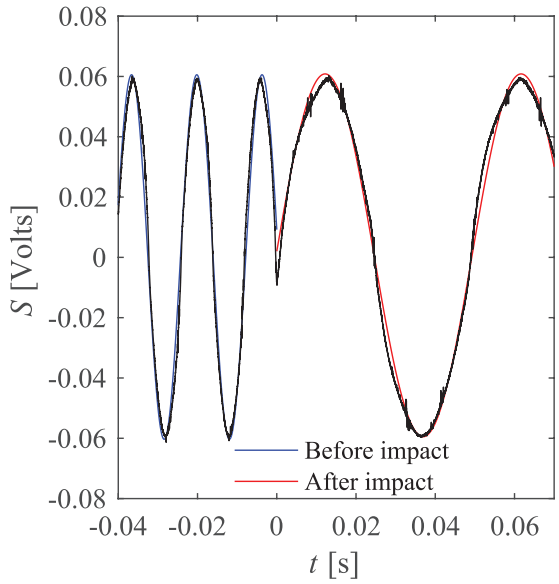

Figure 8. Photodiode signal (S) due to the impactor motion. Time (t) is referenced from the moment of impact with the impulse test stand.

The impulse delivered by the impactor was measured based on the velocity of the impactor before and after the strike. The impact speed was found with an optical method illustrated in figure 7. A laser diode and photodiode were situated at opposite sides of the impactor with the optical path perpendicular to the impactor motion. A Ronchi grating (50 line-pair/in) was mounted below the impactor and positioned such that the grating plane intersected the beam in the perpendicular direction. The impactor motion periodically interrupted the beam received by the photodiode, resulting in the signal shown in figure 8.

The speed change of the impactor before and after its collision with the impulse test stand was computed as follows. First, the impact time was determined from the discontinuity in the photodiode signal (figure 8 at $t = 0$). Then, a segment of the photodiode signal before the impact was curve fitted using a sine function. The process was repeated for a segment of the photodiode signal after the impact. The frequency of the photodiode signal before and after the impact was computed from the curve fit parameter and multiplied with the line spacing of the Ronchi grating to determine the impactor speed. The difference of the velocity before and after the impact was multiplied by the total impactor mass (10.8 g) and the impulse delivered by the impactor was found. The impulse uncertainty was computed based on the measurement uncertainty of impactor mass, curve fit uncertainty of the frequency, and uncertainty in the impactor orientation relative to the impulse test stand ($\pm 1°$).

The displacement of the test stand in response to the impactor strike (figure 9(a)) was measured simultaneously with the photodiode signal. The impulse response (equation (14)) was fit to the test stand displacement to determine the modal parameters of the test stand.

The maximum displacement of the test stand was found from the amplitude of the curve fit on the test stand displacement, and the maximum displacement was compared to the impulse delivered by the impactor (figure 9(b)). The slope of the linear fit gave the calibration factor of 4.81 ± 0.13 mN s mm^{-1} (95% confidence based on the uncertainty of the curve fit parameter). This value compares well with the theoretical calibration factor ($m_{eq}\omega_d$) of 4.72 mN s mm^{-1} calculated with the RailPAc mass (109.2 g). Because different rail and rod geometries slightly changed the test stand center of mass, the calibration step was repeated for each rail and rod configuration.

4. Results

4.1. High-speed imaging

The high-speed images of the arc transit for rod and rail configurations gave insight into the effects of electrode spacing and geometry on the arc morphology. The arc is readily identified in the images (figure 10) as a bright filament bridging the gap between the rails or rods.

4.1.1. Rod electrodes. High-speed images for B06 configuration (rods spaced $d = 6.35$ mm) shown in figure 10 reveal a single filament arc moving at high speed along the electrodes. The arc shape changes at different stages of its transit. The arc luminosity is high in the initial stage ($t < 0.25$ ms), and the arc extends to large distances above and below the electrodes. Note also that the arc luminosity is highest near the electrodes due to electric field enhancement near the electrode surfaces [31]. The arc, if viewed from above, can be described as a linear filament in the initial transit images ($t = 0.05$ and $t = 0.25$ ms). The arc shape subsequently deforms into an inverted U-shape ($t = 0.5$ and 0.75 ms) as a result of changes in the Lorentz and aerodynamic forces acting on the arc.

The displacement of the arc between successive images shown in figure 10 is nearly constant due to the constant transit velocity of the arc. The arc decelerates only towards the end of its transit and its shape ($t = 0.75$ ms) shows remarkable

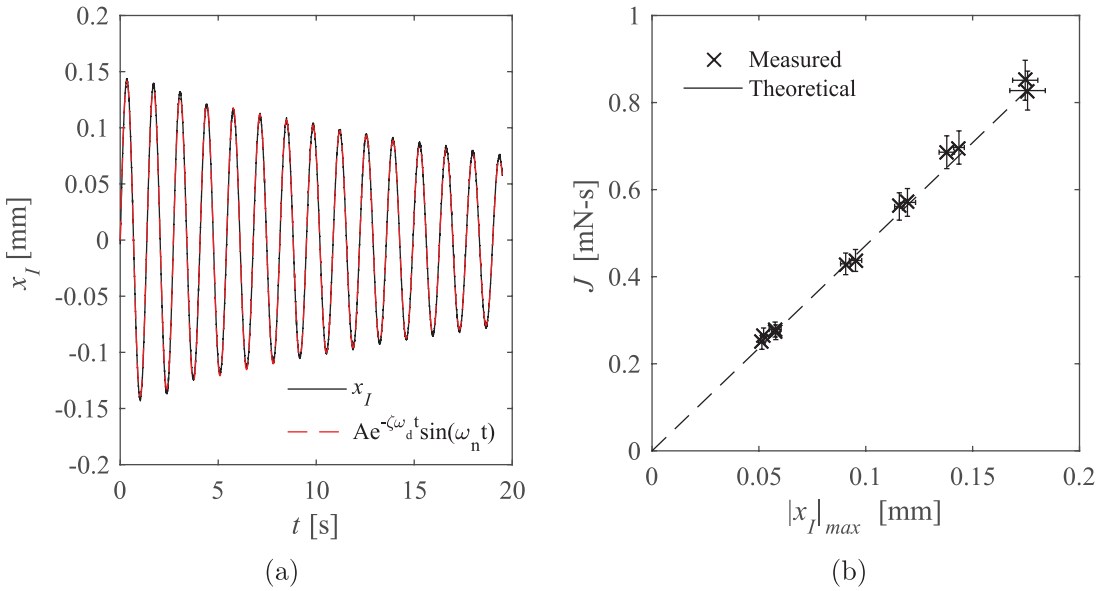

Figure 9. (a) Impulse test stand response to the impactor strike and (b) calibration result for B13 (rod electrodes spaced 12.7 mm apart).

difference compared to the rest of the transit stages. In particular, the arc experiences substantial elongation along the transit direction. This shape change is attributed to the relative velocity between the arc and the surrounding air, where by the induced velocity of the surrounding air behind the arc is higher than the arc transit velocity.

Figure 11 shows the effect of electrode spacing on the arc shape for rod electrodes. The front view of the arc for B02 and B13 configurations (rods with $d = 2$ mm and 12.7 mm) reveals that the extent of the arc above and below the electrodes depends on the electrode spacing. While both configurations host a single filament arc that bridges the gap between the rods, the arc becomes brighter and its extent above and below the electrodes is more significant if the rods are spaced 2 mm apart. The changes in the arc morphology are attributed to the direct interaction between field enhancement regions if the gap width is decreased.

4.1.2. Rail electrodes. Figure 11 shows a dramatic change in the shape of the arc if the electrodes are changed from rods to rails. A significant upward ($\hat{e}_z$-direction) deflection of the arc occurs in the rail case compared to the rod case. The deflection is a result of flush mounted rails because the ceramic in the gap prevents the arc from forming near the RailPAc surface. The physical mechanism behind the deflection was studied by Gray *et al* [20]. They proposed that the initial deflection of the arc away from the insulating gap is provided by gas expansion due to ohmic heating. This initial distortion results in an arc current above the electrode plane and a component of magnetic field collinear to the propagation direction forms. The interaction of the arc current with this magnetic field results in an expansion of the arc above the insulating gap. If the arc elongation is substantial, anchoring can be observed (A13 configuration rails with $d = 12.7$ mm). When the anode root is anchored, the two arc roots produce distinct jets without a visible filament that connects the two jets. If the gap spacing is decreased as demonstrated in A02 configuration (rails with

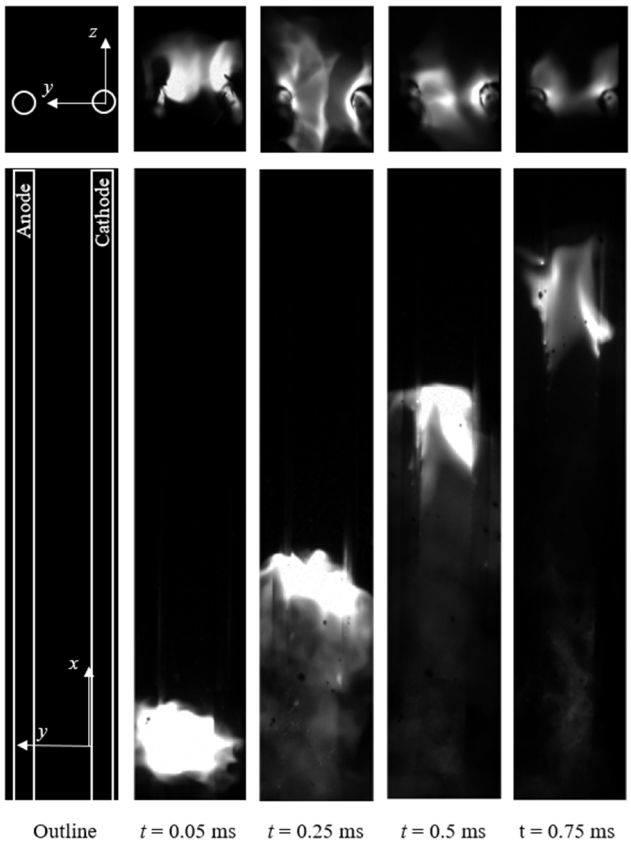

Figure 10. Front and top view of the arc transit for B06 configuration (rod electrodes spaced 6.4 mm apart) at initial capacitor voltage of 240 V. Images time t are referenced from arc initiation at $t = 0$ ms.

$d = 2$ mm), a single filament arc is maintained throughout the transit without anchoring. Unlike the rod electrodes, however, the arc appears much brighter and displays substantial upward deflection. It was concluded by Gray *et al* [21] in their spectroscopy study that most of the arc current is carried by the region bounded by red lines in figure 11, while the remaining

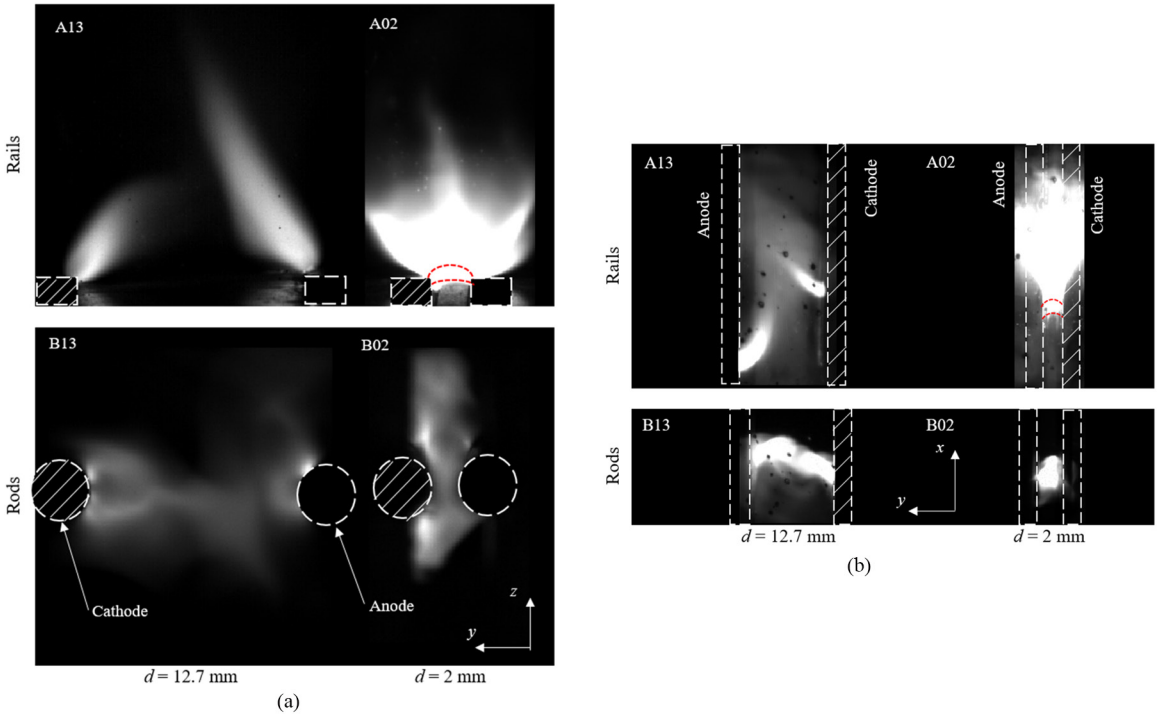

Figure 11. Comparison of arc shapes for A02, A13, B02, and B13 configurations (rod and rail electrodes with 2 mm and 12.7 mm gap distance) at $t = 0.5$ ms, referenced from the arc initiation. Initial capacitor voltage for all cases is 240 V. (a) Front view and (b) top view of the arc. Note for A02, red line is provided to readily distinguish the current carrying portion of the arc.

region of the arc is a thermal interaction between the surrounding air and the arc.

The images clearly show that the arc shape, and therefore the spatial distribution of current density, is sensitive to the electrode geometry. Equation (10) predicts that if the current density is varied, there is a corresponding change in the volumetric Lorentz force that the arc experiences. Since the region of highest induced magnetic field exists near the electrodes, it can be argued that a single filament arc will experience the largest volumetric Lorentz force in the region close to the electrodes. If the arc can be confined to this region, one can expect an increase in the actuation authority of a RailPAc. The exact effect of arc shape on the actuation authority can be understood if the arc shape is viewed in context of the actuation authority measurements.

4.2. Electrical measurements

The current waveform as well as the capacitor voltage (figure 12) show that the circuit behaves similarly to a series RLC circuit with a discharge duration of ∼1.4 ms. The initial spike in the rail voltage and current trace corresponds to the vaporization of the aluminum fuse wire. Note that the capacitor voltage decays exponentially from the initial voltage to the final rail voltage, suggesting that the total energy discharged by the capacitor is a function of the rail voltage. An initiation energy of ∼15 J was obtained by integrating the product of rail voltage and current over the vaporization duration ($t < 0.1$ ms). The arc voltage of ∼70 V is relatively constant throughout the discharge, despite rapid variation in the arc current. The arc resistance varies due to the changes

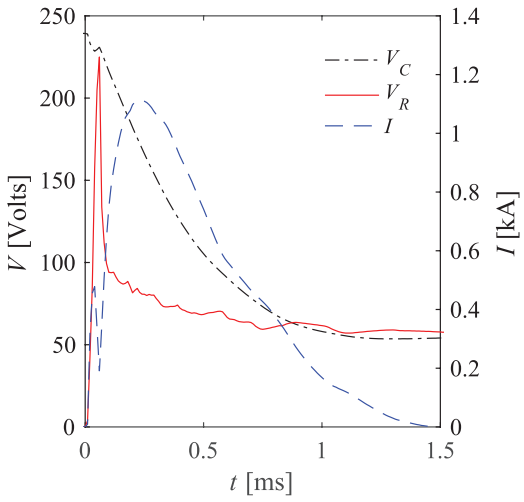

Figure 12. Current and voltage traces of B13 configuration (rod electrodes with $d = 12.7$ mm) at initial capacitor voltage of 220 V.

in the arc shape and small fluctuations in the arc voltage can be observed as a result. While the peak current measured for the electrode spacing of 12.7 mm and V_{ci} of 220 V was ∼1 kA, the peak current varied from ∼500 A to ∼1.4 kA depending on the electrode geometry. For example, the highest current was achieved for narrowly spaced electrodes with V_{ci} of 240 V.

The arc resistance (figure 13(a)) decreases with increasing arc current due to the negative differential resistance of the arc [31]. The arc resistance was modeled using a factorial form,

$$R_a = \frac{a}{I + b} \tag{16}$$

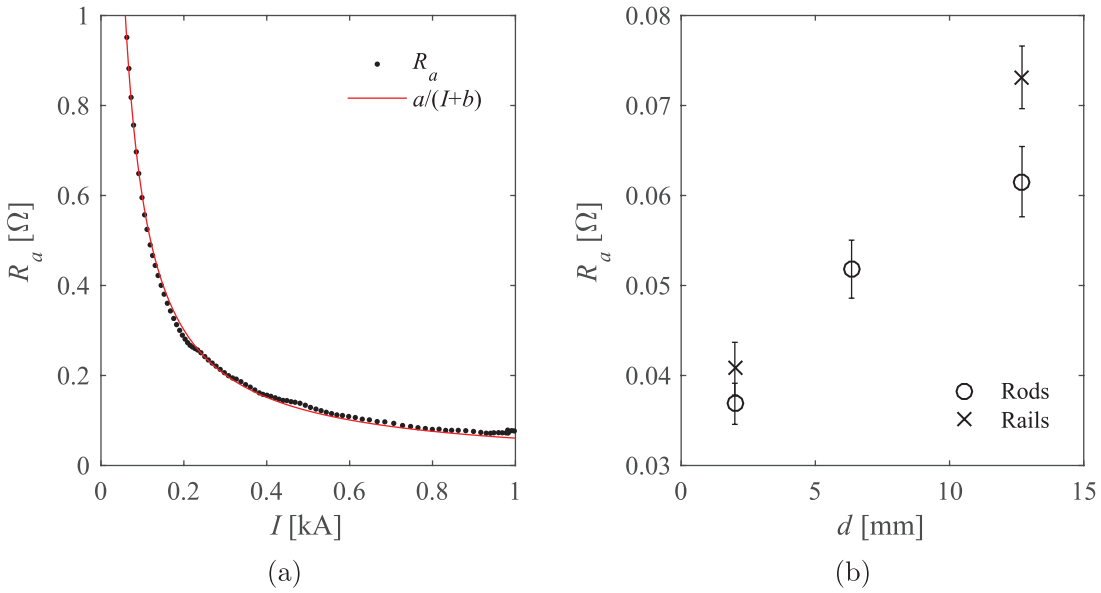

Figure 13. (a) Arc resistance (R_a) as a function of arc current (I) for B13 configuration (rods spaced 12.7 mm apart) at initial capacitor voltage of 240 V. (b) Arc resistance (at $I = 1$ kA) as a function of electrode spacing (d).

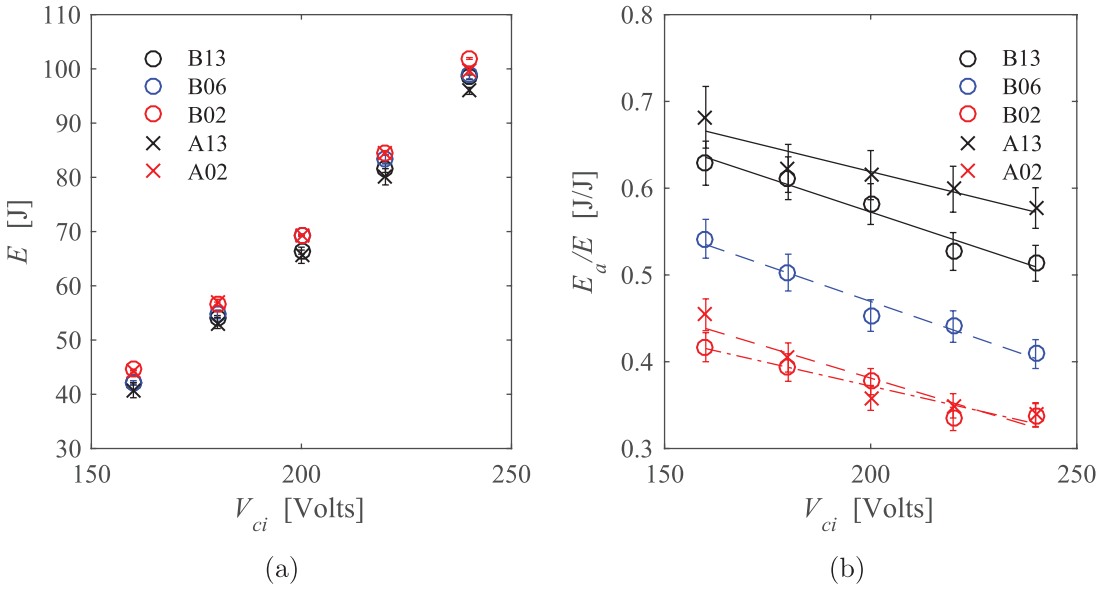

Figure 14. (a) Total energy discharged from the capacitor (E) and (b) energy dissipated by the arc (E_a) as a function of initial capacitor voltage (V_{ci}). The curves in (b) are linear regression lines.

where, a and b are curve fit parameters. This form was assumed based on the observation that the rail voltage (product of current and arc resistance) does not vary significantly over the discharge duration shortly after the arc initiation ($t > 0.14$ ms). For the B13 configuration shown in figure 13(a) ($d = 12.7$ mm rod and $V_{ci} = 240$ V), the arc resistance was calculated from the current and rail voltage after $t > 0.14$ ms. Then, the curve fit coefficients of $a = 61 \pm 2\,\Omega$ kA and $b = 2 \pm 3$ kA were obtained. The physical significance of each fitting parameter is currently unknown and will be investigated in future studies.

The measured arc resistances for different rail and rod geometries cannot be compared directly because their value depends on the arc current. Instead, equation (16) was curve fit to all test cases and the arc resistance at 1 kA was interpolated (figure 13(b)). It can be seen that R_a is independent of arc and electrode shape (i.e. rod and rail cross section), but depends on electrode spacing and anchoring.

4.2.1. Rod electrodes. The results obtained from rod electrodes provide insight into the effect of electrode spacing on the arc resistance. As shown in figure 13(b), the arc resistance increases with the electrode spacing. It was expected from the spectroscopy measurements by Gray *et al* [20] that the arc resistance would be linearly proportional to the arc length because their measurements showed that the arc temperature, and by extension the arc resistivity, does not vary significantly as a function of the arc current. The non-linearity in the plot of arc resistance versus gap distance is due to the fact that the gap distance is not a true measure of the arc length. Indeed, the high-speed images of the arc reveal that the arc maintains a

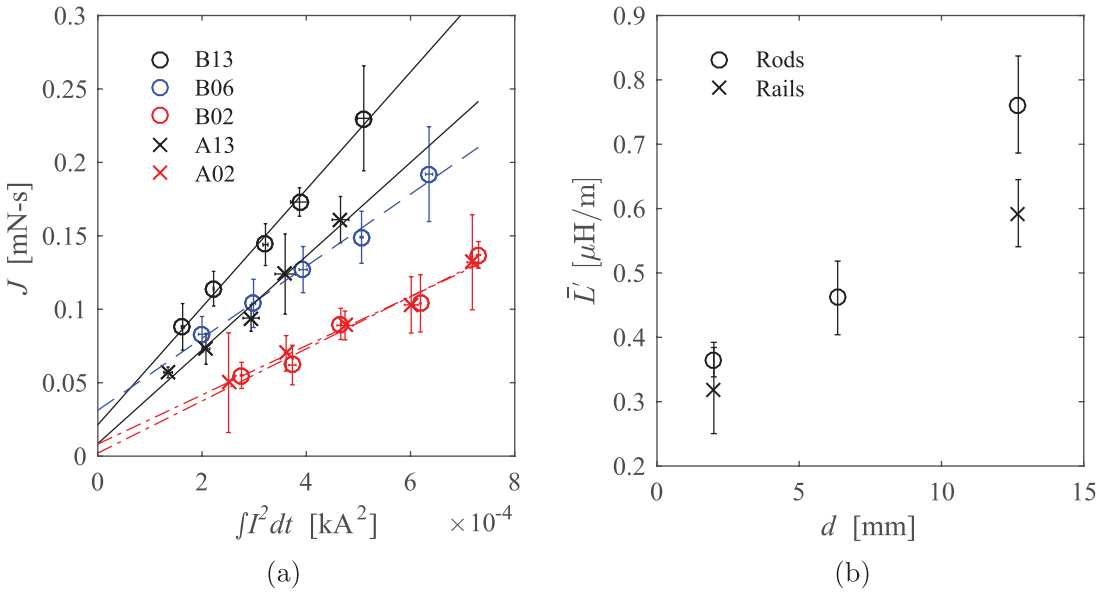

Figure 15. (a) RailPAc impulse (J) as a function of action integral and (b) inductance gradient as a function of gap spacing (d) for rail and rod cases. The curves in (a) are linear regression lines.

U-shape along the plane formed by the parallel rods, such that the actual arc length is longer than the gap width.

As shown in figure 14(a), the total energy discharged by the capacitor is linearly proportional to the initial capacitor voltage and relatively insensitive to the RailPAc geometry. Larger discharge energy is achieved for narrowly spaced rods compared to the widely spaced rods. Highest total energy discharged by the capacitor was ~100 J at V_{ci} of 240 V, which represents almost 100% of the initial capacitor energy.

The ratio of arc energy to total energy is shown as a function of the initial capacitor voltage in figure 14(b). Note that the energy ratio is sensitive to the electrode spacing. For example, at V_{ci} of 160 V, almost 70% of total energy is dissipated by the arc at large electrode spacing ($d = 12.7$ mm), while only 40% is dissipated by the arc at small electrode spacing ($d = 2$ mm).This is explained by the fact that the increase in electrode spacing results in longer arc length, such that the total power dissipated increases.

The peak current increases with initial capacitor voltage because the initial charge stored in the capacitor increases. In comparison to the non-linear arc resistance, the resistance of passive elements of the RailPAc circuit is a constant value that is independent of the arc current. The power dissipated by both the arc and the passive elements scales quadratically with the arc current. However, the power dissipated by the arc scales at a reduced rate compared to the passive elements due to the relationship between resistance and current shown in figure 13(a). The difference in dissipated power causes the proportion of the energy consumed by the arc to decrease in comparison to that of the passive elements in the RailPAc circuit as the current is increased. Since it is desirable to have most of the capacitor energy be delivered to the arc, the energy ratio reveals that a large arc current is inefficient in terms of transferring energy into the arc. Although equation (10) shows that the body force increases quadratically with the arc current, the increase in actuation authority comes at a cost of reduced efficiency.

4.2.2. Rail electrodes. The effect of ceramic gap and anchoring on the electrical properties of the arc can be determined from the electrical measurements on the RailPAc with rail electrodes. The arc resistances for the rail configurations (figure 13(b)) increase with the gap distance in a similar manner to the rod configurations. The arc resistance for rail configuration is higher than that of the rod due to elongation of the arc along the $\hat{e}_z$-direction as a result of upward deflection of the arc away from the ceramic surface. The difference in arc resistance between rail and rod configurations is larger for the wide gap ($d = 12.7$ mm) compared to the narrow gap ($d = 2$ mm). The difference is attributed to anchoring and asymmetric transit of the arc roots that cause further elongation of the arc.

Figure 14(a) shows that the total discharge energies for the rail configurations are equivalent to those of the rod configurations. However, the energy ratio (figure 14(b)) is sensitive to anchoring. Note that if anchoring is not present (A02 and B02—rail and rod electrodes with $d = 2$ mm), the energy ratio does not vary significantly between rail and rod configurations. However, if anchoring is present (A13 and B13—rail and rod electrodes with $d = 12.7$ mm), the rail configuration has higher energy ratio than the rod configuration. The difference is again attributed to the elongation of the arc due to asymmetric transit.

4.3. Impulse measurements

The effect of arc shape and electrode geometry on the actuation authority of the RailPAc was studied with impulse measurements (figure 15). As expected from equation (11), the total impulse scales linearly with the action integral (figure 15(a)) and the inductance gradient can be determined from its slope (figure 15(b)).

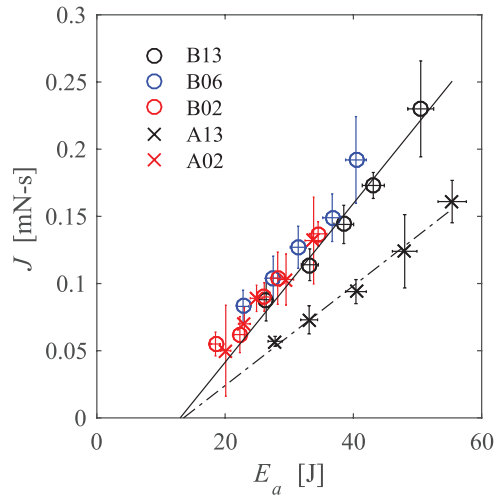

Figure 16. RailPAc scaling law comparing impulse (J) produced for a given energy dissipated by the arc (E_a). The curves are linear regression lines.

4.3.1. Rod electrodes. As shown in figure 15(a), the impulse produced by rod electrodes increases with the electrode gap. If the total impulse is divided by the electrode spacing, the highest impulse per unit length for B13 configuration (rods spaced $d = 12.7$ mm) is 18 mN s m^{-1}. At the same action integral value, the impulse per unit length for B07 and B02 configurations (rods spaced $d = 6.35$ mm and $d = 2$ mm) are 23 mN s m^{-1} and 46 mN s m^{-1}, respectively. Therefore, the impulse per unit length increases with decreasing gap width, even though the total impulse decreases with decreasing gap width. These trends are consistent with the fact that the magnitude of magnetic field in the space between the electrodes is inversely proportional to the distance away from the electrode, such that the contribution from volumetric body force near the electrodes is higher than the contribution from the center of the electrode gap.

The actuation authority can be characterized by examining the inductance gradient in the context of electrode gap (figure 15(b)). If rods have narrow gap ($d = 2$ mm), the inductance gradient is 0.35 μH m^{-1}, while at wider gap ($d = 12.7$ mm), the inductance gradient is 0.75 μH m^{-1}. Therefore, the inductance gradient increases with increasing gap width.

When the impulse is viewed as a function of arc energy, the result is invariant with respect to the gap distance (figure 16). All the results for rod electrodes collapse into a linear line. Note that the slope of impulse versus arc energy is related to the following proportionality constant,

$$\frac{J}{E_a} \sim \frac{\bar{L}'}{R_a}. \tag{17}$$

This relationship was obtained by recognizing that both the impulse and arc energy scale linearly with the action integral. Note that the two proportionality constants, R_a and $\bar{L}'$, represent the arc energy generated for a given electrical input and proportion of the arc energy expended to generate impulse, respectively. As shown in figures 13(b) and 15(b), these values have a weak non-linear relationship with respect to the gap distance. The results show that scaling law does not vary significantly for different gap spacing, if the electrode and arc shapes are held constant.

4.3.2. Rail electrodes. The effect of anchoring on the RailPAc actuation authority can be examined if the measured inductance gradients (figure 15(b)) between rail and rod geometries are compared at the same gap distance. Consider the impulse generated by A13 and B13 configurations (rails and rods spaced 12.7 mm). The inductance gradient for rail electrodes is 0.59 μH m^{-1}, which is 21% less than the actuation authority of the rod electrodes. If anchoring is suppressed in the rail configuration by moving the electrodes close together to 2 mm (A02), then the measured inductance gradient is 0.33 μH m^{-1}, which is only about 6% smaller than that of the rod configuration. Thus, the actuation authority of a RailPAc can be improved if anchoring can be suppressed.

Figure 16 shows that the RailPAc with rail electrodes with small spacing (A02) has a same scaling law as that of the rod electrodes. This trend is readily explained from the high-speed images of the arc. Recall that the narrow rails force the arc to be in proximity of the electrodes and suppress anchoring. If this smooth transit and arc shape can be maintained, the scaling law is invariant to the electrode geometry. If anchoring is present; however, the impulse per unit energy decreases to about half of the smooth transit cases. The high-speed images clearly show that the transit behavior and the arc shape for A13 configuration (rail with 12.7 mm gap spacing) is substantially different than those of other configurations. The arc morphology, therefore, has an impact on the impulse that a RailPAc produces for a given energy input. In particular, anchoring is undesirable for designing an efficient actuator capable of exerting high actuation authority.

5. Summary and conclusions

In summary, the effects of anchoring and arc morphology on the RailPAc actuation authority were studied. The images of the arc revealed that a moving arc under Lorentz force does not transit smoothly along the electrodes as a single filament arc. Indeed, if the RailPAc is designed with the electrodes flush-mounted to the ceramic surface (referred to as the rail configuration), the anode root anchors to the electrode and its motion appears as discrete jumps. If the gap width is decreased to ~2 mm, anchoring is suppressed and the arc transits as a single filament arc. Anchoring can also be controlled by removing the ceramic in the gap. By arranging the electrodes in free-floating rod configuration, anchoring is prevented irrespective of the gap width. The study mounted the RailPAc with rail and rod electrodes on an impulse test stand to evaluate the effect of anchoring on the actuation authority and efficiency of a RailPAc.

The RailPAc with rod electrodes produce a single filament arc which varies its shape throughout the transit. The change in the arc shape is attributed to the variations in aerodynamic and Lorentz forces acting on the arc. Note that the force variation is expected due to the changes in relative velocity between the arc and the neutral gas. To gain

insight into the effect of different electrical input (arc current) and RailPAc design (electrode spacing), the efficiency of a RailPAc was analyzed with the energy ratio (defined as the ratio of arc energy to the total energy discharged by the capacitor) and the inductance gradient. Inductance gradient is a convenient scalar that quantifies how much Lorentz force is produced for a given electrical input. In the absence of anchoring, the energy ratio decreases with larger arc current. Hence, increasing the actuation authority with larger arc current comes at a cost of reduced efficiency, since the proportion of energy dissipated by the arc compared to the total energy decreases with increasing arc current. The impulse measurements showed that the inductance gradient increases with increasing gap width, but the impulse per gap width decreases. When the impulse measurements are compared to the arc energy, the impulse produced for a given arc energy is invariant with respect to the electrode spacing, if smooth transit can be maintained.

The rail electrodes produce an arc with a significant upward deflection with distinct jets emanating from the roots. This deflection is attributed to the presence of an insulating gap between the electrodes. The arc continues its upward motion due to the thermal expansion and the Lorentz force. If the electrode width is reduced to $\sim$2 mm, the distinct jets collapse into a single filament arc that transits without anchoring. Therefore, it is clear from the high-speed images that the formation of jets is related to anchoring, although deeper insight into the physical mechanism requires further study. The comparison of arc resistance, as well as arc energy, for rail and rod configurations demonstrates that the anchoring behavior increases the energy dissipated by the arc. However, the impulse produced by the RailPAc with rail electrodes is less than that of the rod electrodes. In particular, anchoring in rail electrodes reduces the inductance gradient of a RailPAc by 21%. In addition, the impulse produced per arc energy decreases in comparison to the smooth transit behavior. The degradation in actuation authority of rail compared to rod configurations can be reduced by decreasing the rail gap and achieving a smooth transit of the arc in a manner similar to the rod configuration.

It can be concluded from the study that the actuation authority of a RailPAc must not be increased with larger arc current or increasing the electrode spacing. These solutions result in reduced efficiency due to resistive losses and anchoring. Instead, a maximum electrode gap that achieves smooth transit of the arc should be used to maximize efficiency and actuation authority. Further increase in RailPAc actuation authority can be achieved by considering some methods to increase the RailPAc inductance gradient. In the present analysis, the RailPAc represents a single turn inductor, whereby the arc current flows from one rail, jumps across the gap through the arc, and returns to the power supply via the opposite rail. By introducing additional loops of wire beneath the rails or rods, the inductance gradient of a RailPAc geometry can be increased. This solution may provide multiplicative improvement in the actuation authority compared to the cases presented in this paper.

Acknowledgment

This material is based upon work supported by, or in part by, the US Army Research Laboratory and the US Army Research Office under contract/grant number W911NF1410226.

References

[1] Corke T C, Enloe C L and Wilkinson S P 2010 Dielectric barrier discharge plasma actuators for flow control *Annu. Rev. Fluid Mech.* **42** 505
[2] Caruana D 2010 Plasmas for aerodynamic control *Plasma Phys. Control. Fusion* **52** 124045
[3] Enloe C L, Mclaughlin T E, VanDyken R D, Kachner K D, Jumper E J and Corke T C 2004 Mechanisms and responses of a single dielectric barrier plasma actuator: plasma morphology *AIAA J.* **42** 589
[4] Enloe C L, Mclaughlin T E, VanDyken R D, Kachner K D, Jumper E J, Corke T C, Post M and Haddad O 2004 Mechanisms and responses of a single dielectric barrier plasma actuator: geometric effects *AIAA J.* **42** 595
[5] Likhanskii A V, Shneider M N, Macheret S O and Miles R B 2007 Modeling of dielectric barrier discharge plasma actuators driven by repetitive nanosecond pulses *Phys. Plasmas* **14** 073501
[6] Patel M P, Vasudevan S, Corke T C and Suchomel C F 2008 Modeling of dielectric barrier discharge plasma actuators driven by repetitive nanosecond pulses *J. Aircr.* **45** 223
[7] Henoch C and Stace J 1995 Experimental investigation of a salt water turbulent boundary layer modified by an applied streamwise magnetohydrodynamic body force *Phys. Fluids* **7** 1371
[8] Macheret S O, Shneider M N and Miles R B 2004 Analysis of magnetohydrodynamic control of scramjet inlets *AIAA J.* **42** 2303
[9] Palm P, Meyer R, Rich J W and Adamovich I V 2003 Nonequilibrium radio frequency discharge plasma effect on conical shock wave $M = 25$ flow *AIAA J.* **41** 465
[10] Grossman K R, Cybyk B Z, Rigling M C and VanWie D M 2004 Characterization of sparkjet actuators for flow control *42nd AIAA Aerospace Sciences Meeting and Exhibit (Reno, NV)* AIAA 2004-0089
[11] Utkin Y G, Saurabh K, Kim J-H, Kastner J, Adamovich I V and Samimy M 2006 Developement and use of localized arc filament plasma acutuators for high-speed flow control *J. Phys. D: Appl. Phys.* **40** 685
[12] Post M L and Corke T C 2006 Separation control using plasma actuators: dynamic stall vortex control on oscillating airfoil *AIAA J.* **44** 3125
[13] Little J 2009 High-lift airfoil trailing edge separation control using a single dielectric barrier discharge plasma actuator *Exp. Fluids* **48** 521
[14] Roupassov D V, Nikipelov A, Nudnova M M and Starikovskii A Y 2009 Flow separation control by plasma actuator with nanosecond pulsed-periodic discharge *AIAA J.* **47** 521
[15] Likhanskii A V, Shneider M N, Opaits D F, Miles R B and Macheret S O 2010 Limitations of the DBD effects on the external flow *48th AIAA Aerospace Sciences Meeting Including the New Horizons Forum and Aerospace Exposition. (Orlando, FL)* p 470
[16] Boeuf J P, Lagmich Y, Unfer T, Callegari T and Pitchford L C 2007 Electrohydrodynamic force in dielectric barrier discharge plasma actuators *J. Phys. D: Appl. Phys.* **40** 652
[17] Pafford B, Sirohi J and Raja L L 2013 Propagating-arc magnetohydrodynamic plasma actuator for directional

high-authority flow control in atmospheric air *J. Phys. D: Appl. Phys.* **46** 485208
[18] Choi Y, Gray M, Sirohi J and Raja L L 2017 Measurement of velocity induced by a propagating arc magneto-hydrodynamic plasma actuator *55th AIAA Aerospace Sciences Meeting (Grapevine, TX)* AIAA 2017–0156
[19] Choi Y, Sirohi J and Raja L L 2015 Measurement of transient force produced by a propagating arc magnetohydrodynamic plasma actuator in quiescent atmospheric air *J. Phys. D: Appl. Phys.* **48** 425204
[20] Gray M, Choi Y, Sirohi J and Raja L L 2015 Structure of propagating arc in a magnetohydrodynamic rail plasma actuator *J. Phys. D: Appl. Phys.* **49** 015202
[21] Gray M, Choi Y, Sirohi J and Raja L L 2017 Experimental investigation of the internal structure and dynamic behavior of the rail plasma actuator arc *55th AIAA Aerospace Sciences Meeting (Grapevine, TX)* AIAA 2017–0158
[22] Weldon W F, Driga M D and Woodson H H 1986 Recoil in electromagnetic railguns *IEEE Trans. Magn.* **6** 1808
[23] Ray P K 2007 Eddy current effects in the laminated containment structure of railguns *IEEE Trans. Magn.* **43** 150
[24] Department of Defense Handbook 1983 *Electrical Grounding for Aircraft Safety* (*MIL-HDBK-274(AS)*) (Washington, DC: US Dept. of Defense)
[25] Koizumik H, Komurasaki K and Arakawa Y 2004 Development of thrust stand for low impulse measurement from microthrusters *Rev. Sci. Instrum.* **75** 3185
[26] Elias P Q and Castera P 2013 Measurement of the impulse produced by a pulsed surface discharge actuator in air *J. Phys. D: Appl. Phys.* **46** 365204
[27] Liu J, Ju L and Blair D B 1997 Vibration isolation performance of an ultra-low frequency folded pendulum resonator *Phys. Lett.* A **228** 243
[28] Witalis E A 1995 Origin, location, magnitude and consequences of recoil in the plasma armature railgun *IEE P-Sci. Meas. Tech.* **142** 197
[29] Sabedin D R 1997 Conservation of momentum and recoil in the railgun *IEEE Trans. Magn.* **33** 599
[30] Kathe E L 2001 Recoil consideration for railguns *IEEE Trans. Magn.* **37** 425
[31] Raizer Y P 1991 *Gas Discharge Physics* (New York: Springer)